X-ray diffraction reveals two structural transitions in szomolnokite

OLIVIA S. PARDO^{1,*}, VASILIJE V. DOBROSAVLJEVIC¹, TYLER PEREZ^{1,2}, WOLFGANG STURHAHN¹, ZHENXIAN LIU³, GEORGE R. ROSSMAN¹, AND JENNIFER M. JACKSON¹

¹Division of Geological and Planetary Sciences, California Institute of Technology, 1200 E. California Boulevard, Pasadena, California 91125, U.S.A.

²Now at Johns Hopkins University, 3400 N. Charles Street, Baltimore, Maryland 21218, U.S.A.
³Department of Physics, University of Illinois at Chicago, Chicago, Illinois 60607, U.S.A.

ABSTRACT

Hydrated sulfates have been identified and studied in a wide variety of environments on Earth, Mars, and the icy satellites of the solar system. The subsurface presence of hydrous sulfur-bearing phases to any extent necessitates a better understanding of their thermodynamic and elastic properties at pressure. End-member experimental and computational data are lacking and are needed to accurately model hydrous, sulfur-bearing planetary interiors. In this work, high-pressure X-ray diffraction (XRD) and synchrotron Fourier-transform infrared (FTIR) measurements were conducted on szomolnokite (FeSO₄·H₂O) up to ~83 and 24 GPa, respectively. This study finds a monoclinic-triclinic (C2/c to $P\overline{1}$) structural phase transition occurring in szomolnokite between 5.0(1) and 6.6(1) GPa and a previously unknown triclinic-monoclinic ($P\overline{1}$ to $P2_1$) structural transition occurring between 12.7(3) and 16.8(3) GPa. The high-pressure transition was identified by the appearance of distinct reflections in the XRD patterns that cannot be attributed to a second phase related to the dissociation of the $P\bar{1}$ phase, and it is further characterized by increased H₂O bonding within the structure. We fit third-order Birch-Murnaghan equations of state for each of the three phases identified in our data and refit published data to compare the elastic parameters of szomolnokite, kieserite (MgSO₄·H₂O), and blödite (Na₂Mg(SO₄)₂·4H₂O). At ambient pressure, szomolnokite is less compressible than blödite and more than kieserite, but by 7 GPa both szomolnokite and kieserite have approximately the same bulk modulus, while blödite's remains lower than both phases up to 20 GPa. These results indicate the stability of szomolnokite's high-pressure monoclinic phase and the retention of water within the structure up to pressures found in planetary deep interiors.

Keywords: Szomolnokite, hydrated sulfates, high pressure, X-ray diffraction, infrared spectroscopy, equation of state

Introduction

Szomolnokite (FeSO₄·H₂O) is a hydrous, ferrous iron-sulfate belonging to the kieserite group of minerals which is composed of monoclinic hydrated metal sulfates. On Earth, szomolnokite and other metal sulfates naturally occur as weathering products of pyrite or pyrrhotite and have been studied in relation to evaporate deposits, hydrothermal systems, and mine waste (Chou et al. 2013; Dyar et al. 2013; Machado de Oliveira et al. 2019). Because ferrous iron-sulfates can host numerous other divalent metals, such as Cu and Mn, they are capable of releasing significant amounts of other trace metals into the surrounding environment (Chou et al. 2013). Hydrated sulfates have also been discussed in relation to volatile cycling within the mantle and their role as potential oxidizing agents upon release of their volatiles at depth (Bénard et al. 2018; Schwarzenbach et al. 2018; Li et al. 2021).

Hydrated sulfates are not only studied in relation to surface and subsurface processes on Earth but have more recently become of interest for other planetary bodies, after sulfate minerals, including szomolnokite, were detected on Mars using absorption spectroscopy (Bishop et al. 2009; King and McLennan 2010; Chou et al. 2013). This has led to hydrated sulfates' importance as potential hosts for water at depth, their use in determining past hydrological activity on the surface of Mars, and their role in volatile and sulfur cycling (Lichtenberg et al. 2010; Wendt et al. 2011; McCanta et al. 2014; Franz et al. 2019). On Venus, sulfates are hypothesized to exist at the surface and crust (Barsukov et al. 1982). Additionally, hydrous metal sulfates have been proposed to exist on the surface of icy moons in our solar system owing to their spectral similarity between laboratory measurements and remote observations (Dalton and Pitman 2012; Ligier et al. 2019; Trumbo et al. 2020).

Hydrated sulfates have been characterized under a range of pressures and temperatures. Szomolnokite has a monoclinic crystal structure (space group C2/c) at ambient conditions as determined by early X-ray diffraction (XRD) measurements on powdered szomolnokite (Pistorius 1960), and ambient-pressure, single-crystal XRD measurements (Wildner and Giester 1991; Giester et al. 1994) (see Table 1). At ambient conditions, szomolnokite belongs to the kieserite group, which consists of monoclinic, hydrous metal sulfates ($MSO_4 \cdot H_2O$). The kieserite

^{*} E-mail: opardo@caltech.edu. Orcid 0000-0003-3964-9272

structure consists of corner-sharing $[MO_4(H_2O)]^6$ units running parallel to the crystallographic c-axis. Most recently, single-crystal, high-pressure XRD measurements combined with Raman and Fourier-transform infrared (FTIR) spectroscopy up to 9.2 GPa found a monoclinic-triclinic structural phase transition at 6.154(1) GPa and retention of structurally bound H_2O throughout the pressure range investigated (Meusburger et al. 2019). An analogous transition was observed to occur in the Mg-end-member kieserite (MgSO₄·H₂O) at lower pressures (Meusburger et al. 2020), the Ni-end-member dworknikite (NiSO₄·H₂O) (Ende et al. 2020), and the Co-end-member (CoSO₄·H₂O) (Wildner et al. 2021).

Other studies conducted on hydrated sulfates have focused on decomposition induced by moderate pressure and variable temperature. Neutron powder diffraction of deuterated MgSO₄·11D₂O, the deuterated analog of meridianiite, was used to explore pressures between 0.1-1000 MPa and temperatures between 150-280 K (Fortes et al. 2017). At ambient conditions meridianiite is triclinic (space group $P\overline{1}$) with a structural phase transition and decomposition of MgSO₄·11D₂O to ice VI + MgSO₄·9D₂O occurring at 0.9 GPa and 240 K. The relatively dehydrated MgSO₄·9D₂O is monoclinic (space group $P2_1/c$). Additional work has focused on the decomposition of hydrous, Cu-, Ni-, Zn-, and Fe-bearing sulfates as a function of temperature using X-ray photoelectron spectroscopy, scanning electron microscopy/X-ray microanalysis, thermogravimetric analysis, diffuse reflectance infrared Fourier transform spectroscopy, and X-ray diffraction (Siriwardane et al. 1999). Results for the FeSO₄·7H₂O sample used in these decomposition experiments indicate dehydration initiating at temperatures up to 200 °C with the decomposition of sulfate initiating around 500 °C, producing Fe₂O₃ (Siriwardane et al. 1999).

Phase relations of MSO₄·nH₂O systems have been explored at high pressure and temperature. One experiment on the MgSO₄-H₂O system at temperatures ranging from 298–500 K and pressures up to 4.5 GPa found a eutectic system with six distinct phases (Nakamura and Ohtani 2011). Using X-ray diffraction and micro-Raman spectrometry, MgSO₄·H₂O, MgSO₄·6H₂O, and MgSO₄·7H₂O were among the identified phases that coexisted with high-pressure ice polymorphs. In situ X-ray diffraction and Mössbauer spectroscopy were used to investigate the two endmembers and 10 intermediate compositions of the FeSO₄·H₂O-CuSO₄·H₂O solid solution series (Giester et al. 1994). At ambient conditions $CuSO_4 \cdot H_2O$ is triclinic (space group $P\overline{1}$). Giester et al. (1994) found that FeSO₄·H₂O-CuSO₄·H₂O compositions with >20 mol% Cu are triclinic (space group $P\overline{1}$), distorted from the monoclinic (space group C2/c) structure of FeSO₄·H₂O. Additionally, the FeSO₄·H₂O-MgSO₄·H₂O solid-solution series was examined under ambient and martian surface temperature conditions using X-ray diffraction, Fourier transform infrared spectroscopy, and Raman spectroscopy (Talla and Wildner 2019). Linear changes in lattice parameters, crystal structure, and the positions of absorption bands were observed as a function of Fe-content and deviated from linear behavior with decreasing temperature.

The pressure dependence of hydrated sulfate properties, in particular szomolnokite, has received less attention. Their stability at depth determines, in part, their volatile transport capabilities and geophysical behavior. For example, structural phase transitions influence the dynamics and seismic signatures within planetary interiors, especially for phase transitions exhibiting large volume changes. As an end-member hydrated sulfate, szomolnokite provides a means to study the effects of iron on phase stabilities and elastic properties, which are the focus of this study. Characterization of end-member species, like szomolnokite, under high-pressure conditions will help develop our understanding of the complex behavior of this class of minerals and their role in planetary interior environments.

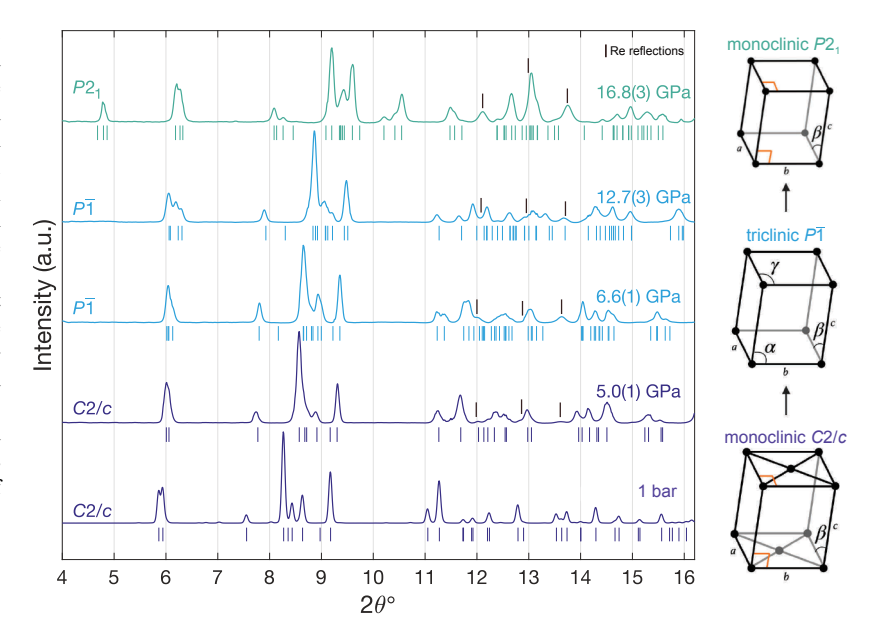
In this study, we focus on the effect of pressure on the crystal structure of szomolnokite and associated elastic properties utilizing X-ray powder diffraction and synchrotron infrared spectroscopy. We present a detailed analysis and equation of state fits of X-ray powder diffraction measurements conducted in the pressure range of 0-83 GPa. Within this pressure interval, we find that the data are compatible with two different structural phase transitions. We term the high-pressure phases β -Sz and γ -Sz. The phase transition from the C2/c to $P\overline{1}$ space group (β -Sz) occurs between 5.0(1) and 6.6(1) GPa, and the transition from the $P\overline{1}$ to $P2_1$ space group (γ -Sz) occurs between 12.7(3) and 16.8(3) GPa, where the number in parentheses is the estimated pressure uncertainty for the last significant digit. Synchrotron infrared spectra reveal that for each phase transition, structurally bound H₂O is retained in the unit cell. We fit finite-strain equations of state to the data for each polymorph, compare them against previous work, and present our new results on the γ-Sz phase.

METHODS

Powdered szomolnokite was synthesized through collaboration with Isoflex (FeSO₄·H₂O, using 96% ⁵⁷Fe) and loaded into a symmetric diamond-anvil cell (DAC) using a helium pressure medium to achieve hydrostatic pressure conditions. Diamond anvils (250 µm flat culet diameter, 300 µm bevel) were mounted on either a tungsten carbide seat (upstream side of the DAC) or a cubic boron nitride seat (downstream side of the DAC) to maximize the accessible 2θ range for X-ray diffraction measurements. Using an electric discharge machine, a 150 µm (diameter) hole was drilled into a pre-indented (50 µm thick) rhenium gasket, which served as the sample chamber. The powdered szomolnokite sample that was loaded had the approximate shape of a disk with the following dimensions: 85 µm in diameter and \sim 50 μm thick, together with pressure gauges (one ruby sphere and a small amount of tungsten powder). Helium was loaded and sealed into the sample chamber, with a ruby fluorescence signal indicating a pressure of 0.44 GPa in the sample chamber. The sample chamber diameter decreased by ~20 um immediately after helium loading at 0.44 GPa, and the approximate volume ratio of helium to sample and pressure gauges (tungsten powder and a ruby sphere) was ~3:1. In situ pressure determination was achieved using X-ray diffraction (XRD) measurements of the tungsten powder at each compression point (Dorogokupets and Oganov 2006). The tungsten and sample were not co-located; thus, pressure determination and uncertainties were estimated by collecting an XRD pattern of the tungsten powder immediately before (and after) collecting an XRD pattern of the szomolnokite sample. The reported experiment pressure was taken to be the standard error of these two pressure measurements.

X-ray diffraction measurements were conducted at beamline 12.2.2 of the Advanced Light Source at Lawrence Berkeley National Laboratory up to 83 GPa at room temperature. An X-ray wavelength of 0.4972 Å and a beam size of 20 μ m were used on a sample size of ~85 μ m in diameter. Ambient-pressure (1 bar), room-temperature measurements were performed on powdered szomolnokite in a Kapton tube. The sample-to-detector distance and tilt were calibrated using a CeO₂ standard. The integration of raw diffraction patterns was performed using the Dioptas software (Prescher and Prakapenka 2015). Saturated regions and diamond reflections were manually masked for each XRD pattern in Dioptas before being exported to GSAS-II for Pawley refinement (Toby and Von Dreele 2013; Prescher and Prakapenka 2015). Although the observable 20 range extends up to 28.7°, we restrict our refinement analysis to the range of ~4 \leq 20(°) \leq 24 to simplify background removal.

FIGURE 1. Integrated diffraction patterns at five selected compression points are plotted with a vertical offset: the ambient-pressure pattern and the diffraction patterns before and after each structural phase transition. Each pattern has undergone background removal and the intensity of each pattern has been normalized for easier comparison between the different compression points such that the maximum value of each pattern is equal to one. Reflections for the crystal structures used to fit each pattern are plotted below each respective pattern. The phase transition from the C2/c to $P\overline{1}$ space group occurs between 5.0(1) and 6.6(1) GPa, and the transition from the P1 to P2₁ space group occurs between 12.7(3) and 16.8(3) GPa. The unit-cell transformations are described schematically to the right of the diffraction patterns (see Online Materials1 Figure S2 for relative cell size and orientation). (Color online.)



High-pressure synchrotron infrared compression and decompression measurements up to 24 GPa were conducted at beamline 22-IR-1 at the National Synchrotron Light Source II at Brookhaven National Laboratory. Powdered szomolnokite was loaded into a diamond-anvil cell with a KBr pressure medium and ruby sphere for pressure determination. Synchrotron FTIR spectroscopic measurements were taken using a Bruker Vertex 80v FTIR spectrometer and a custom IR microscope system with a wide-band MCT detector from 400–5000 cm⁻¹.

Third-order Birch Murnaghan equation of state fits for each of the three structural polymorphs identified in this study were carried out using the MINUTI (MINeral physics UTIlities) open-source software (Sturhahn 2020). Three approaches were used to fit each of the polymorphs: (1) K_{70} was fixed, and V_{70} and K_{70} were varied without the use of priors; (2) K_{70} , V_{70} , and K_{70} were varied without priors; and (3) K_{70} , V_0 , and K_{70} were all varied with priors. See Table 2 for select details on initial values and choice of prior values. The C2/c and $P\overline{1}$ single-crystal szomolnokite data of Meusburger et al. (2019) were refit using the same procedure described above. This allows our work to be directly compared with the low-pressure polymorphs, including pressure-dependent error ellipses, to visualize the correlation between V, K_7 , and K_7' for each fit result.

RESULTS

Figure 1 presents select X-ray diffraction patterns with predicted reflections corresponding to each structural phase identified in this work. An overview of the full integrated diffraction pattern data set is displayed in the Online Materials¹ Figure S1. The C2/c structure fits the XRD patterns from 0-5 GPa, after which a second-order structural phase transition occurs, and the patterns are well described by the $P\overline{1}$ structure. Following the nomenclature used for the same C2/c to PĪ transition for kieserite (MgSO₄·H₂O) (see Meusburger et al. 2020), we term the FeSO₄·H₂O $P\overline{1}$ structure β -Sz. Between 12.7(3)–16.8(3) GPa β-Sz undergoes a previously unknown transformation into a $P2_1$ structure, now termed γ -Sz, that fits the data until the last compression point measured at 83 GPa. See Online Materials¹ Table S1 for the full set of refined lattice parameters resulting from Pawley refinement in GSAS-II. Figure 1 shows a schematic of the three unit cells associated with the C2/c, $P\overline{1}$, and P2₁ phases. See Online Materials¹ Figure S2 for the relative size and orientation of each cell. High-pressure FTIR measurements indicate retention of water and the strengthening of hydrogen bonds within the unit cell of each phase up to pressures of 24 GPa.

C2/c to β -Sz $P\overline{1}$: 1 bar to 12.7 GPa

The ambient-pressure diffraction pattern was fitted using the lattice parameters and space group C2/c reported from an earlier study on szomolnokite (Giester et al. 1994; Meusburger et al. 2019) as starting values in the refinement process. The ambient-pressure lattice parameters derived in this work are generally in good agreement with those reported from recent XRD experiments, with the exception of those reported by Pistorius (1960) (Table 1). With increasing pressure, the space group C2/c provides a good fit to the XRD patterns up to 5 GPa. After this pressure, peak splitting is observed, and the patterns can no longer be fit using the predicted reflections for the monoclinic C2/c structure. Using the cell-search capability in GSAS-II, selected crystal structures and space groups were tested to find the best-fit crystal structure model for the high-pressure phase. This analysis finds a structural phase transition occurring from the monoclinic C2/c to triclinic $P\overline{1}$ structure between 5.0(1) and 6.6(1) GPa.

The XRD patterns collected from 6.6(1) GPa to 12.7(3) GPa are well described by the triclinic structure ($P\overline{1}$). The monoclinic-triclinic transition pressure interval in our study brackets the transition pressure reported from recent XRD measurements (Giester et al. 1994; Meusburger et al. 2019). Meusburger et al. (2019) performed single-crystal XRD measurements on szomolnokite up to 9.2 GPa, finding a second-order, monoclinic-triclinic structural phase transition occurring between 5.951(5)-6.154(1) GPa. They

 TABLE 1. Szomolnokite ambient-condition lattice parameters

a (ų)	<i>b</i> (ų)	c (ų)	β (°)	V (ų)	Reference
7.624(9)	7.469(9)	7.123(9)	115.86(3)	391.70	Pistorius (1960) ^a
7.078(3)	7.549(3)	7.773(3)	118.65(2)	364.45	Wildner and Giester (1991) ^b
7.084	7.550	7.779	118.63	365.16	Giester et al. (1994) ^a
7.086(1)	7.555(1)	7.780(1)	118.61(1)	365.63(8)	Talla and Wildner (2019) ^b
7.0823(2)	7.5525(2)	7.7786(5)	118.631(3)	365.23(30)	Meusburger et al. (2019) ^b
7.086(2)	7.5497(3)	7.779(2)	118.656(3)	365.15(3)	This work ^a

Notes: Uncertainties are given in parentheses for the last significant digit(s). ^a Powder X-ray diffraction.

^b Single-crystal X-ray diffraction.

TABLE 2. Equation of state fit parameters and results

Phase	V ₀ (Å ³)	K₀ (GPa)	K' ₇₀	X ²					
S	zomolnokite (F	eSO ₄ ·H ₂ O)	C2/c						
Fixed: K' ₇₀	[365.23 0.30]	[45.2 5]	[6.7]	0.93					
Fit: <i>V</i> ₀ , <i>K</i> ₀	365.13(2)	45.2(4)	[0.7]						
Fit: V_0 , K_0 , K'_{70}	[365.23 0.30]	[45.2 5]	[6.7 2]	0.65					
	365.14(2)	44.5(5)	7.5(5)	0.03					
Refit of published data	[365.23 0.30]	[45.2 5]	[6.7 2]	0.53ª					
•	365.23(2) ^a	45.2(2)a	6.8(1) ^a	0.53 ^b					
Fit: V_0 , K_0 , K'_{70}	365.2(3) ^b	45.2(2) ^b	6.7(1)b	0.55					
Szomolnokite (FeSO ₄ ·H₂O) P1									
Fixed: K'_{70}	[367 0.4]	[45.11 5]	[5.4]	0.14					
Fit: V_0 , K_0	367.02(9)	45.5(2)							
Fit: V_0 , K_0 , K'_{70}	[367 0.4]	[45.11 5]	[5.4 2]	0.09					
	367.02(9)	46.3(6)	5.1(2)	0.09					
Refit of published data	[367 0.4]	[45.11 5]	[5.4 2]	1.72ª					
	367.0(4) ^a	45(1)a	5.4(2)a	0.93 ^b					
Fit: V_0 , K_0 , K'_{70}	367.0(4) ^b	45.1(6) ^b	5.4 (fixed) ^b	, 0.55					
Szomolnokite (FeSO ₄ ·H ₂ O) P2 ₁									
Fit: V_0 , K_0 , K'_{70}	[365 15]	[45 5]	[5.4 2]	1.03					
	357(2)	44(2)	5.8(1)	1.05					
	serite (MgSO₄·l	H₂O): C2/c a	nd <i>P</i> 1						
C2/c	[355.5 0.4]	[48.1 2]	[8.1 2]	0.63°					
Refit of published data	355.5(3) ^c	48.5(5) ^c	7.8(5) ^c	0.60 ^d					
Fit: V_0 , K_0 , K'_{70}	355.5(4) ^d	48.1(5) ^d	8.1(6) ^d	0.00					
P1	[355.8 0.4]	[49.3 2]	[4.8 2]	1.01 ^c 1.14 ^d					
Refit of published data	355.8(2) ^c	49.3(6) ^c	4.8(1) ^c						
Fit: V_0 , K_0 , K'_{70}	356(2) ^d	49(6) ^d	5(1) ^d						
	Blödite (Na₂M	g(SO ₄) ₂ ·4H ₂							
$P2_1/a$	[496.6 0.4]	[36 2]	[5.1 2]	4.82					
Refit of published data	496.5(2) ^e	36.0(7) ^e	5.1(2) ^e	Not Reported ^f					
Fit: V_0 , K_0 , K'_{70}	496.9(7) ^f	36(1) ^f	5.1(4) ^f	Not heported					

Notes: Notation explanation for columns V_0 , K_0 , K_{70} , [A B] X(Y): starting value of A with a prior window of B, and best-fit value of X with an error of Y. [A]: fixed parameter at value of A.

- ^a This work's results from refitting the data of Meusburger et al. (2019).
- ^b As-reported results in Meusburger et al. (2019).
- ^c This work's results from refitting the data of Meusburger et al. (2020).
- ^d As-reported results in Meusburger et al. (2020).
- ^e This work's results from refitting the data of Comodi et al. (2014).
- f As-reported results in Comodi et al. (2014).

identify distortion in the crystal lattice after the phase transition, which creates a second, distinct octahedral site within the crystal structure. A comparison between our low-pressure monoclinic and high-pressure triclinic (β -Sz) lattice parameters and those reported by Meusburger et al. (2019) is shown in Figure 2. The structural parameters of β -Sz are transformed into the monoclinic C2/c space group for both data sets to allow for easier comparison [see Giester et al. (1994) for details of this transformation].

The unit-cell volume values agree well with the single-crystal data at all overlapping pressures, with more deviation occurring between the reported lattice parameters. The a-parameter agrees well up to \sim 2 GPa, where it begins to deviate (up to \sim 0.06 Å difference) and follows a steeper pressure-dependence trend compared to Meusburger et al. (2019). The b-parameter in both studies follow the same general trend, but in our work, it appears to decrease linearly vs. parabolically in the C2/c phase. In the β -Sz phase the differences between b-parameters increase by approximately double (from ~ 0.01 to ~ 0.02 Å) with increasing pressure. Our values are higher than the single-crystal work and further diverge as pressure increases. The c-parameter in both studies agrees the best out of the three unit-cell lengths up to 6.6 GPa, just past the β-Sz phase transition. After this pressure, our c-parameter values trend lower than the single-crystal work and intersect the b-parameter at \sim 8.8 GPa. The b and c parameters, as reported by Meusburger et al. (2019), indicate they would also intersect but at higher pressures than our data. Axial ratio trends for unit-cell lengths a, b, and c are plotted in Online Materials¹ Figure S3.

The unit-cell angles α , β , and γ across the entire pressure range of this work, together with the parameters reported by Meusburger et al. (2019), are shown in panels b and c of Figure 2. The α and γ angles in the C2/c and β -Sz phase are fixed at 90°, characteristic of the monoclinic structure. For easier comparison between the three phases, the β -Sz data are transformed into the monoclinic setting using the cell transformation tool in GSAS-II, using the transformation matrix as described in Giester et al. (1994). The transformation provides a description of the cell in the monoclinic structure by allowing the α and γ angles to be \sim 90°. Lattice parameters in the $P\overline{1}$ space group are reported in Online Materials¹ Table S3. For both our data and the transformed $P\overline{1}$ data reported by Meusburger et al. (2019) α remains approximately constant, with our values scattering around 90°, while γ increases by \sim 2° throughout the β -Sz stability field.

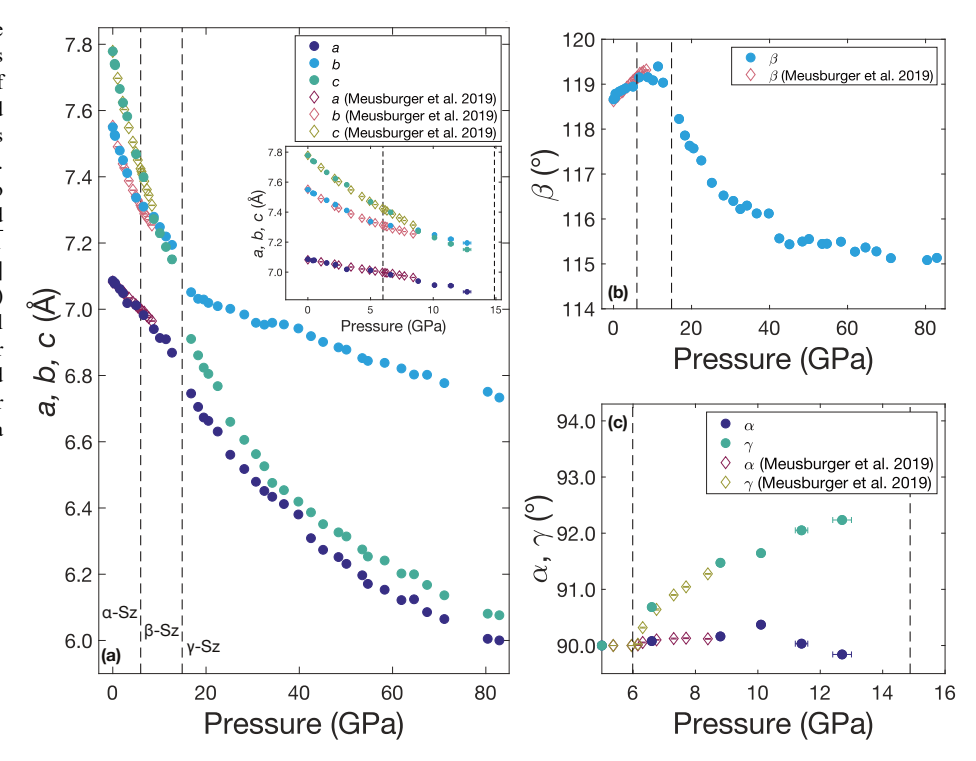
γ-Sz P2₁: 16.8–83 GPa

At 16.8 GPa, the $P\overline{1}$ space group cannot describe the XRD pattern due to the appearance of intense peaks where no $P\overline{1}$ reflections are predicted (e.g., at $\sim 10.5^{\circ} 2\theta$), and the disappearance or merging of triclinic-assigned peaks (see Online Materials1 Fig. S4 for reflections predicted by the $P\overline{1}$ space group at 16.8 GPa). These significant changes in the pattern at 16.8(3) GPa indicate the likelihood that a structural phase transition is occurring. A cell search was again performed to find the best-fit crystal structure and space group. The results of this search indicated that at 16.8(3) GPa, β-Sz undergoes a phase transition from triclinic $P\overline{1}$ to a primitive monoclinic lattice. We select $P2_1$ as the best-fitting space group (see discussion below) and term this new phase γ-Sz. Upon further compression, the XRD data are compatible with the $P2_1$ structure up to the highest pressure in this study, 83 GPa. Figure 1 displays selected X-ray diffraction patterns highlighting the ambient pressure pattern and the two structural phase transitions occurring between 5.0(1)-6.6(1) GPa and 12.7(3)-16.8(3) GPa.

At 16.8(3) GPa, there are several new reflections with a larger $\partial 2\theta/\partial P$ dependence compared to other reflections. These reflections cannot be attributed to other materials in the sample chamber (W, Al₂O₃, He, or Re). The decomposition of β -Sz was considered, but these additional reflections cannot be attributed to H₂O ice VI-VIII, Fe₂O₃, or other iron sulfate/hydroxyl mixtures. However, direct comparison of various iron sulfate/hydroxyl mixtures at these experimental pressures is difficult without available high-pressure XRD data for such phases. In Online Materials¹ Figure S4 we demonstrate that the theoretical high-pressure phase of SO₂ does not account for the new reflections (Zhang et al. 2020). While this is not an exhaustive list of possible phases, the shift of the additional reflections as a function of pressure is well described by a primitive monoclinic space group, and thus, we do not attribute these new reflections to a separate phase.

This work tested many possible crystal structures and space groups to identify the best-fitting structural model for the γ -Sz phase transition at 16.8(3) GPa. The $P\overline{1}$ and P1 space groups do not account for several peak positions in the γ -Sz phase, including

FIGURE 2. The lattice parameters determined from this work are plotted as a function of pressure: (a) a, b, c, (b) β , and (c) α and γ . Lattice parameters reported by Meusburger et al. (2019) up to 9.2 GPa are also plotted for comparison. Dashed lines indicate the C2/c to $P\overline{1}$ [between 5.0(1) and 6.6(1) GPa] and $P\overline{1}$ to $P2_1$ [between 12.7(3) and 16.8(3) GPa] structural transitions. Lattice parameters for the $P\overline{1}$ cell have been transformed into the monoclinic setting for easier comparison across the data set. (Color online.)



the complete absence of the cluster of peaks between 10° and 11° 20. A triclinic cell with a larger unit-cell volume compared to the last-calculated C2/c volume could be a possible solution, but due to the inability to extract atomic positions within the unit cell and choose a cell with consistent density relative to β -Sz, we do not consider triclinic cells as candidate structures. Nevertheless, the data are well fit by a primitive monoclinic structure of comparable size to the monoclinic-setting β -Sz unit cell and thus exhibits reflections that can be attributed to a higher symmetry phase.

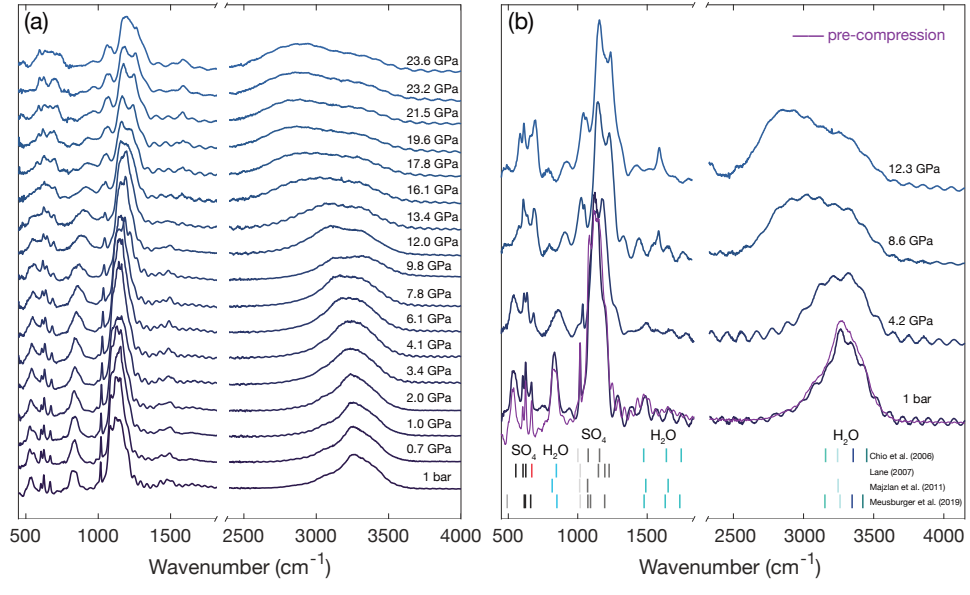
Online Materials¹ Figures S5-S6 plots reflections for the C2/m (Online Materials Fig. S5 only), $P2_1$, $P2_1/m$, P2/m, P2/c, $P2_1/c$, P2, Pm, and Pc groups resulting from Pawley refinement fits at 16.8 and 67.4 GPa. Face-centered monoclinic structures do not fit the data, as seen in Online Materials¹ Figure S5 with the example of the C2/m space group, thus only primitive monoclinic structures were examined in detail. The eight monoclinic-P space groups tested here all exhibit almost identical reflection sets except for a few reflection regions located at $\sim 5^{\circ}$, $\sim 8.45^{\circ}$, \sim 12.15°, \sim 14.1°, and \sim 20.3° 20 at 16.8 GPa. The peaks present at ~12.15° and ~14.1° 2θ for space groups such as Pm and P2/cadditionally overlap with Re peaks from the strained gasket detected by tails of the X-ray focused beam. Online Materials1 Figure S5 contains a caked diffraction image at 16.8 GPa zoomed into the 2θ region containing two Re peaks at ~12.15° and $\sim 14.1^{\circ} 2\theta$. The Re peaks are diffuse, and the image does not indicate the presence of overlapping szomolnokite reflections. For this reason, only space groups without reflections overlapping with the ~12.15° 20 Re peak were considered: $P2_1$, $P2_1/m$, P2/m, and $P2_1/c$.

Upon increasing pressure, it is clear that more than one reflection is needed to fit the peaks at \sim 5.1° 20 and \sim 9.4° 20, which

only includes the $P2_1$, $P2_1/m$, and P2/m space groups, which are almost identical. With the broad and overlapping nature of the peaks characteristic of high-pressure powder data, it is difficult to make any further distinction based on the quality of fits (see Online Materials¹ Fig. S7 for R_w discussion). Out of these three space groups, the $P2_1$ phase is chosen as the reported space group due to it being the lowest symmetry. However, we fit the entire γ -Sz pressure region with both the $P2_1$ and P2/m space groups and find that the resulting equation of state parameters are the same within error. Lattice parameters for all space groups fit are given in Online Materials¹ Table S1–S3. We stress that the γ-Sz phase may be attributed to several primitive monoclinic space groups, and although we choose the P2₁ space group for discussion within this manuscript, future work is needed to accurately determine the atomic positions within the unit cell of γ-Sz and allow for the selection of a unique space group.

The stability of γ-Sz and the retention of H₂O within its crystal structure after the high-pressure phase transition is further supported by high-pressure synchrotron infrared measurements. Figure 3 displays measured FTIR spectra in the frequency range of 500-4000 cm⁻¹ of 17 compression measurements up to 24 GPa and four decompression measurements. Assigned SO₄²⁻ and H₂O bands from several infrared spectroscopy measurements on szomolnokite are plotted at the bottom of the right panel in Figure 3 (Chio et al. 2007; Lane 2007; Majzlan et al. 2011; Meusburger et al. 2019). Spectral features indicate increased hydrogen bonding environments and strength in the crystal structure due to the broadening and pressure-dependent shift of H₂O bands in the ~3000 cm⁻¹ range toward lower wavenumbers with increasing pressure. The shift toward lower wavenumbers, combined with increasingly broadened H₂O bands without the addition of new spectral features in the ~3000 cm⁻¹ region with increasing pres-

FIGURE 3. Panel a plots infrared spectra for the 17 compression points up to 24 GPa. Pressure-dependent shift of the H2O bands initially centered around 3200 cm⁻¹ at 1 bar toward lower wavenumbers with increasing pressure indicates increased hydrogen bonding within the crystal structure. Panel b plots the four decompression measurements. The precompression 1 bar pattern is also plotted against the postdecompression 1 bar pattern for comparison. The bottom of panel b plots assigned bands as reported by their four respective studies. The high-frequency noise present in all spectra is due to interference from the diamond anvils within the sample chamber. (Color online.)



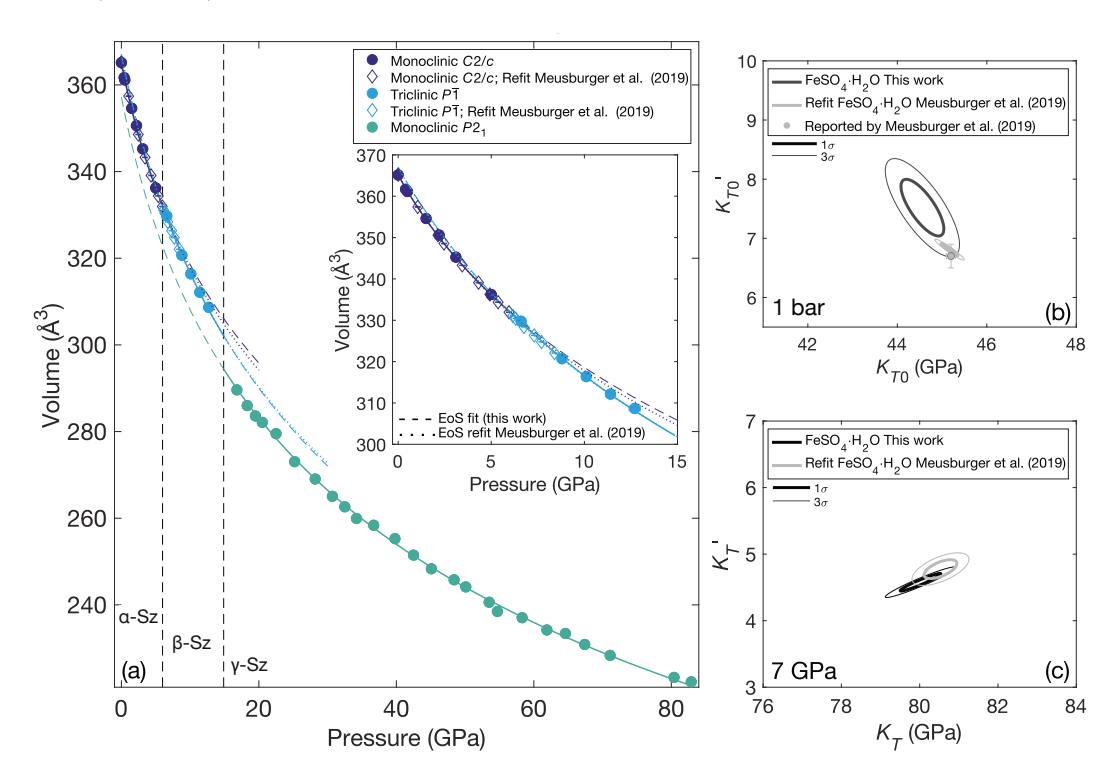
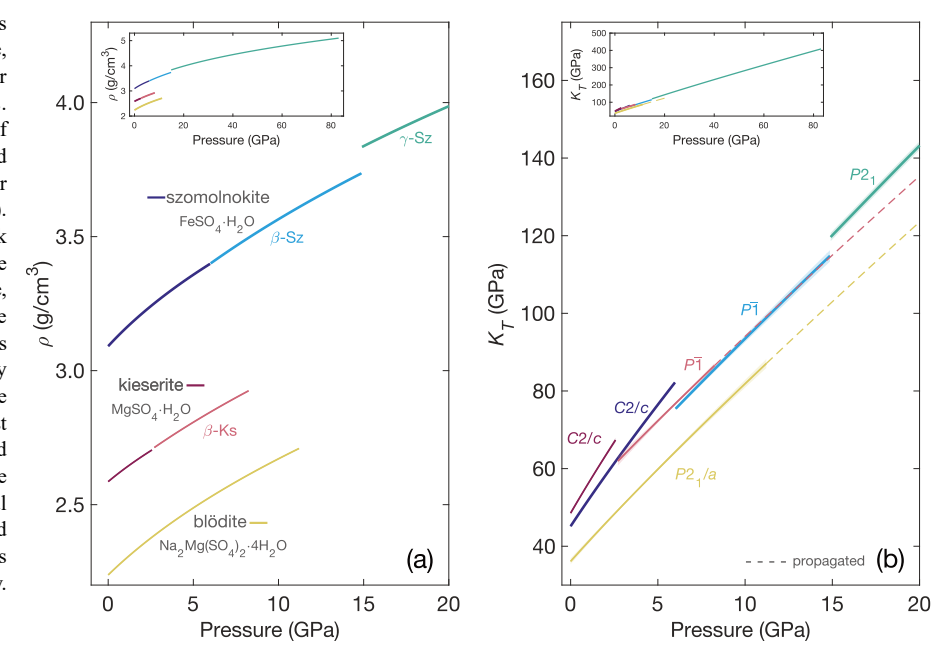


FIGURE 4. Panel **a** plots volume data with equation of state fits for the three C2/c, $P\overline{1}$, and $P2_1$ phases for this study (solid circles, dashed lines) and the refits of the single-crystal study for the C2/c and $P\overline{1}$ phases (open diamonds, dotted lines). Volume measurements for these two phases match well between these two studies. Our work extends the $P\overline{1}$ stability field until at least 12.7(3) GPa. 1 σ and 3 σ error ellipses are plotted in panel (**b**) K'_{70} vs. K_{70} error ellipse at 1 bar, in addition to reported values by Meusburger et al. (2019), and panel (**c**) K'_{7} vs. K_{7} at 7 GPa for our data and refit of Meusburger et al. (2019). (Color online.)

sure, does not indicate the addition of $\rm H_2O$ groups into the unit cell, suggesting that the monohydrated structure is the most stable at high pressure. Upon decompression, all bands in the spectra return to the same wavenumber positions and relative intensities measured at ambient pressure prior to compression.

The β -Sz $P\overline{1}$ to γ -Sz $P2_1$ transition exhibits a noticeable volume drop (\sim 6% decrease over a \sim 4 GPa pressure interval, see Fig. 4). The volume drop is characterized by a sharp decrease in the c-axis unit-cell length (0.25 Å), and moderate drops in the a- and b-axis lengths (0.12 and 0.14 Å, respectively) over the \sim 4 GPa interval

FIGURE 5. (a) Calculated densities output by MINUTI for szomolnokite, kieserite, and blödite and their respective high-pressure phases. The high-pressure polymorphs of szomolnokite and kieserite are plotted as different colors (blue and green for szomolnokite, pale red for kieserite). (b) MINUTI results for the bulk modulus K_T as a function of pressure are plotted for szomolnokite, kieserite, and blödite and their respective high-pressure phases. Space groups for each polymorph are indicated by adjacent color-coded labels. Errors are reported as the shaded regions, most visible in the γ -Sz $P2_1$ phase. Dashed lines indicate extrapolation above previously reported experimental pressures. It is unknown if β-Ks and blödite undergo phase transitions above 8.3 and 11.2 GPa, respectively. (Color online.)



bracketing the phase transition. At higher pressures, the β angle begins to decrease and continues until ~45 GPa. At this pressure, the β angle plateaus until the last compression point. The β angle decreases from 118.2° to 114.8° from the start of the γ -Sz phase transition at 16.8(3) GPa to the last measured compression point at 83 GPa. Over the γ -Sz pressure range, the a and c axis lengths compress at approximately the same rate beginning at ~45 GPa, corresponding with the plateauing of the β angle. This behavior may occur over the pressure range in which the Fe atoms undergo a broad spin transition between 45 and 95 GPa. See Perez et al. (2020) for further discussion regarding spin transition models for szomolnokite and its high-pressure phases.

EQUATIONS OF STATE

Equation of state (EoS) fits from MINUTI using priors and pressure-volume data for szomolnokite, and its β-Sz and γ-Sz high-pressure polymorphs are presented in Figure 4a. We compare our refit of the single-crystal data from Meusburger et al. (2019) for the C2/c and β -Sz $P\overline{1}$ phases. We find that extremely small differences in volume measurements, most likely due to experimental conditions, combined with small volume-error values, produce EoS fit results with statistically different V_0 values (see Online Materials¹ Figures S8–S10 for K_T – V_T error ellipses for each phase). Error ellipses provide a valuable method for visualizing the uncertainty and correlation between model parameters in an EoS fit. Figure 4b and 4c plot $K_T - K_T$ at 1 bar and 7 GPa. Error ellipses for our refit results of Meusburger et al. (2019), along with their reported EoS fit values at 1 bar are also plotted. We find that for the C2/c phase at 1 bar both studies exhibit a strong negative correlation between K_T and K_T , but these parameters are positively correlated by 7 GPa in the β-Sz phase.

EoS model parameters are commonly reported at 1 bar, regardless if the data are representative of phases whose stability fields only exist at high pressure. In this work, we demonstrate the

importance of comparing the elastic properties of high-pressure phases within their respective stability fields. In Online Materials¹ Figure S11 we plot our refit K_T vs. K_T' error ellipse results for the Mg-hydrated sulfate end-member kieserite [Mg(SO₄)·H₂O] using volume values reported from single-crystal XRD data (Meusburger et al. 2020), and a refit of a single-crystal XRD volume measurements of blödite [Na2Mg(SO4)2·4H2O] (Comodi et al. 2014), a candidate Na-bearing mineral modeled on the surface of Europa (Dalton et al. 2012). We find that at ambient pressure, szomolnokite is less compressible than blödite but more than kieserite. However, by 7 GPa, both szomolnokite and kieserite have undergone C2/c to $P\overline{1}$ structural transitions (into the β -Sz and β -Ks phases, respectively) and have approximately the same bulk modulus value, while blödite remains lower than both phases up to 20 GPa. Figure 5 plots K_T and density as a function of pressure for szomolnokite, kieserite, blödite, and their respective high-pressure phases resulting from our MINUTI EoS fits and re-fits.

Even though β -Ks and β -Sz display similar incompressibilities around 10 GPa, kieserite and β -Ks are much lower in density (Fig. 5). Szomolnokite exhibits a slight density increase across the β -Sz transition but undergoes a sharp increase in density across the γ -Sz transition. Blödite is significantly lower in density than both phases, which is accompanied by its lower bulk modulus across this entire pressure range. It was not observed to undergo a phase transition from its ambient-pressure monoclinic $P2_1/a$ structure up to 11.2 GPa and retains water within the unit cell, exhibiting increased hydrogen bonding with increasing pressure (Comodi et al. 2014).

IMPLICATIONS

Surface measurements and observations of icy satellites in the solar system indicate an abundance of hydrated sulfates on Europa, Ganymede, and Callisto (Dalton et al. 2012; Hibbitts et al. 2019; Cartwright et al. 2020). The relative exogenic vs. endogenic origins of these surface sulfur-bearing ice and salt phases are unclear (Trumbo et al. 2020), but even a purely exogenic sulfur origin could result in subsequent sulfur cycling due to exchange between the icy crust and underlying interior (Vu et al. 2020). The stability and elastic properties of szomolnokite and related phases discussed in this work imply complex pressure and chemical-dependent behavior and, thus, potentially important factors for icy satellite interiors. Within the high-pressure triclinic stability field, β-Sz, and β-Ks exhibit equal incompressibility with drastically different densities, while the addition of Fe into Mg-bearing hydrated sulfates may affect the elastic parameters and increase the depth at which the monoclinic-triclinic transition occurs within sulfate-bearing icy mantles. For smaller icy satellites, where mantle pressures are less than 5 GPa, this transition may not occur at all.

If β -Sz retains its water after the γ -Sz structural transition, as our preliminary FTIR data indicate, the stability of this new high-pressure phase to pressures of at least 83 GPa could have implications for its ability to retain water in planetary deep interiors. However, other obvious factors, such as temperature and coexisting phases, would affect this behavior and are largely unexplored. For example, incorporating Mg into the crystal structure could significantly lower the β-phase transition pressure (Meusburger et al. 2020) and also affect water retention. In particular, future work investigating the effect of temperature on the structural behavior of szomolnokite, its high-pressure β-Sz and γ-Sz phase transitions, and other coexisting and/or hydrous sulfates will deepen our understanding of their ability to retain water at conditions most relevant to icy satellite or terrestrialtype planetary interiors. Future work investigating the electronic and vibrational properties of szomolnokite will further broaden our understanding of the Fe-end-member hydrated sulfate. Such data, including the work presented here, are needed to conduct more complex phase equilibria modeling for planetary interiors in which hydrous sulfates are proposed to exist.

FUNDING

We thank the W.M. Keck Foundation and the National Science Foundation (NSF-CSEDI-EAR-1600956, 2009935) for supporting this work. O.P. acknowledges the support of DOE NNSA SSGF (DE-NA0003960). Work at the National Synchrotron Light Source II at Brookhaven National Laboratory was funded by the Department of Energy (DEAC98- 06CH10886). The use of the 22-IR-1 beamline was supported by COMPRES under NSF Cooperative Agreement EAR 11-57758 and CDAC (DE-FC03-03N00144).

REFERENCES CITED

- Barsukov, V.L., Volkov, V.P., and Khodakovsky, I.L. (1982) The crust of Venus: Theoretical models of chemical and mineral composition. Journal of Geophysical Research, 87 (S01), A3, https://doi.org/10.1029/JB087iS01p000A3.
- Bénard, A., Klimm, K., Woodland, A.B., Arculus, R.J., Wilke, M., Botcharnikov, R.E., Shimizu, N., Nebel, O., Rivard, C., and Ionov, D.A. (2018) Oxidising agents in sub-arc mantle melts link slab devolatilisation and arc magmas. Nature Communications, 9, 3500, https://doi.org/10.1038/s41467-018-05804-2.
- Bishop, J.L., Parente, M., Weitz, C.M., Noe Dobrea, E.Z., Roach, L.H., Murchie, S.L., McGuire, P.C., McKeown, N.K., Rossi, C.M., Brown, A.J., and others. (2009) Mineralogy of Juventae Chasma: Sulfates in the light-toned mounds, mafic minerals in the bedrock, and hydrated silica and hydroxylated ferric sulfate on the plateau. Journal of Geophysical Research. 114. F00D09. https://doi.org/10.1029/2009JF003352.
- Cartwright, R.J., Nordheim, T.A., Cruikshank, D.P., Hand, K.P., Roser, J.E., Grundy, W.M., Beddingfield, C.B., and Emery, J.P. (2020) Evidence for sulfur-bearing species on Callisto's leading hemisphere: Sourced from Jupiter's irregular satellites or Io? The Astrophysical Journal. Letters, 902, L38, https://doi.org/10.3847/2041-8213/abbdae.
- Chio, C.H., Sharma, S.K., and Muenow, D.W. (2007) The hydrates and deuterates of

- ferrous sulfate (FeSO₄): A Raman spectroscopic study. Journal of Raman Spectroscopy: JRS, 38, 87–99, https://doi.org/10.1002/jrs.1623.
- Chou, I.-M., Seal, R.R. II, and Wang, A. (2013) The stability of sulfate and hydrated sulfate minerals near ambient conditions and their significance in environmental and planetary sciences. Journal of Asian Earth Sciences, 62, 734–758, https://doi.org/ 10.1016/j.jseaes.2012.11.027.
- Comodi, P., Nazzareni, S., Balić-Žunić, T., Zucchini, A., and Hanfland, M. (2014) The high-pressure behavior of blödite: A synchrotron single-crystal X-ray diffraction study. American Mineralogist, 99, 511–518, https://doi.org/10.2138/am.2014.4640.
- Dalton, J.B., and Pitman, K.M. (2012) Low temperature optical constants of some hydrated sulfates relevant to planetary surfaces. Journal of Geophysical Research. Planets. 117.
- Dalton, J.B., Shirley, J.H., and Kamp, L.W. (2012) Europa's icy bright plains and dark linea: Exogenic and endogenic contributions to composition and surface properties. Journal of Geophysical Research. Planets, 117.
- Dorogokupets, P.I., and Oganov, A.R. (2006) Equations of state of Al, Au, Cu, Pt, Ta, and W and revised ruby pressure scale. Doklady Earth Sciences, 410, 1091–1095, https://doi.org/10.1134/S1028334X06070208.
- Dyar, M.D., Breves, E., Jawin, E., Marchand, G., Nelms, M., O'Connor, V., Peel, S., Rothstein, Y., Sklute, E.C., Lane, M.D., and others. (2013) Mössbauer parameters of iron in sulfate minerals. American Mineralogist, 98, 1943–1965, https://doi.org/ 10.2138/am.2013.4604.
- Ende, M., Kirkkala, T., Loitzenbauer, M., Talla, D., Wildner, M., and Miletich, R. (2020) High-pressure behavior of nickel sulfate monohydrate: Isothermal compressibility, structural polymorphism, and transition pathway. Inorganic Chemistry, 59, 6255–6266, https://doi.org/10.1021/acs.inorgchem.0c00370.
- Fortes, A.D., Fernandez-Alonso, F., Tucker, M., and Wood, I.G. (2017) Isothermal equation of state and high-pressure phase transitions of synthetic meridianiite (MgSO₄·11D₂O) determined by neutron powder diffraction and quasielastic neutron spectroscopy. Acta Crystallographica, B73, 33–46, https://doi.org/10.1107/ S2052520616018254.
- Franz, H.B., King, P.L., and Gaillard, F. (2019) Sulfur on Mars from the Atmosphere to the Core. In J. Filiberto and S.P. Schwenzer, Eds., Volatiles in the martian Crust, p. 119–183. Elsevier.
- Giester, G., Lengauer, C.L., and Redhammer, G.J. (1994) Characterization of the FeSO₄·H₂O-CuSO₄·H₂O solid-solution series, and the nature of poitevinite, (Cu,Fe) SO₄·H₂O. Canadian Mineralogist, 32, 873–884.
- Hibbitts, C.A., Stockstill-Cahill, K., Wing, B., and Paranicas, C. (2019) Color centers in salts—Evidence for the presence of sulfates on Europa. Icarus, 326, 37–47, https:// doi.org/10.1016/j.icarus.2019.02.022.
- King, P.L., and McLennan, S.M. (2010) Sulfur on Mars. Elements (Quebec), 6, 107–112, https://doi.org/10.2113/gselements.6.2.107.
- Lane, M.D. (2007) Mid-infrared emission spectroscopy of sulfate and sulfate-bearing minerals. American Mineralogist, 92, 1–18, https://doi.org/10.2138/am.2007.2170.
- Li, J.-L., Schwarzenbach, E.M., John, T., Ague, J.J., Tassara, S., Gao, J., and Konecke, B.A. (2021) Subduction zone sulfur mobilization and redistribution by intraslab fluid-rock interaction. Geochimica et Cosmochimica Acta, 297, 40–64, https://doi.org/ 10.1016/j.gea.2021.01.011.
- Lichtenberg, K.A., Arvidson, R.E., Morris, R.V., Murchie, S.L., Bishop, J.L., Fernandez Remolar, D., Glotch, T.D., Noe Dobrea, E., Mustard, J.F., Andrews-Hanna, J., and others. (2010) Stratigraphy of hydrated sulfates in the sedimentary deposits of Aram Chaos, Mars. Journal of Geophysical Research, 115, E00D17, https://doi.org/ 10.1029/2009JE003353.
- Ligier, N., Paranicas, C., Carter, J., Poulet, F., Calvin, W.M., Nordheim, T.A., Snodgrass, C., and Ferellec, L. (2019) Surface composition and properties of Ganymede: Updates from ground-based observations with the near-infrared imaging spectrometer SINFONI/VLT/ESO. Icarus, 333, 496–515, https://doi.org/10.1016/ii.carus.2019.06.013.
- Machado de Oliveira, C., Gesser Müller, T., Patricio Ferreira, L., Prado Cechinel, M.A., Peterson, M., and Raupp-Pereira, F. (2019) Valorization of iron pyrite from coal mining in southern Brazil. Journal of Environmental Chemical Engineering, 7, 102931, https://doi.org/10.1016/j.jece.2019.102931.
- Majzlan, J., Alpers, C.N., Koch, C.B., McCleskey, R.B., Myneni, S.C.B., and Neil, J.M. (2011) Vibrational, X-ray absorption, and Mössbauer spectra of sulfate minerals from the weathered massive sulfide deposit at Iron Mountain, California. Chemical Geology, 284, 296–305, https://doi.org/10.1016/j.chemgeo.2011.03.008.
- McCanta, M.C., Dyar, M.D., and Treiman, A.H. (2014) Alteration of Hawaiian basalts under sulfur-rich conditions: Applications to understanding surface-atmosphere interactions on Mars and Venus. American Mineralogist, 99, 291–302, https://doi.org/ 10.2138/am.2014.4584.
- Meusburger, J.M., Ende, M., Talla, D., Wildner, M., and Miletich, R. (2019) Transformation mechanism of the pressure-induced C2/c-to-PT transition in ferrous sulfate monohydrate single crystals. Journal of Solid State Chemistry, 277, 240–252, https://doi.org/10.1016/j.jssc.2019.06.004.
- Meusburger, J.M., Ende, M., Matzinger, P., Talla, D., Miletich, R., and Wildner, M. (2020) Polymorphism of Mg-monohydrate sulfate kieserite under pressure and its occurrence on giant icy jovian satellites. Icarus, 336, 113459, https://doi.org/10.1016/ j.icarus.2019.113459.
- Nakamura, R., and Ohtani, E. (2011) The high-pressure phase relation of the MgSO₄— H₂O system and its implication for the internal structure of Ganymede. Icarus, 211,

American Mineralogist, vol. 108, 2023

- 648-654, https://doi.org/10.1016/j.icarus.2010.08.029.
- Perez, T., Finkelstein, G.J., Pardo, O., Solomatova, N.V., and Jackson, J.M. (2020) A synchrotron Mössbauer spectroscopy study of a hydrated iron-sulfate at high pressures. Minerals (Basel), 10, 146, https://doi.org/10.3390/min10020146.
- Pistorius, W.F.T. (1960) Lattice Constants of FeSO₄·H₂O (artificial szomolnokite) and NiSO₄·H₂O. Bulletin des Sociétés Chimiques Belges, 69, 570–574, https://doi.org/ 10.1002/bscb.19600691106.
- Prescher, C., and Prakapenka, V.B. (2015) DIOPTAS: A program for reduction of twodimensional X-ray diffraction data and data exploration. High Pressure Research, 35, 223–230, https://doi.org/10.1080/08957959.2015.1059835.
- Schwarzenbach, E.M., Caddick, M.J., Petroff, M., Gill, B.C., Cooperdock, E.H.G., and Barnes, J.D. (2018) Sulphur and carbon cycling in the subduction zone mélange. Scientific Reports, 8, 15517, https://doi.org/10.1038/s41598-018-33610-9.
- Siriwardane, R.V., Poston, J.A. Jr., Fisher, E.P., Shen, M.-S., and Miltz, A.L. (1999) Decomposition of the sulfates of copper, iron (II), iron (III), nickel, and zinc: XPS, SEM, DRIFTS, XRD, and TGA study. Applied Surface Science, 152, 219–236, https://doi.org/10.1016/S0169-4332(99)00319-0.
- Sturhahn, W. (2020) MINeral physics UTIlity (MINUTI) open-source software package. http://www.nrixs.com.
- Talla, D., and Wildner, M. (2019) Investigation of the kieserite–szomolnokite solid-solution series, (Mg,Fe)SO₄·H₂O, with relevance to Mars: Crystal chemistry, FTIR, and Raman spectroscopy under ambient and martian temperature conditions. American Mineralogist, 104, 1732–1749, https://doi.org/10.2138/am-2019-6983.
- Toby, B.H. (2006) R factors in Rietveld analysis: How good is good enough? Powder Diffraction, 21, 67–70.
- Toby, B.H., and Von Dreele, R.B. (2013) GSAS-II: The genesis of a modern open-source all purpose crystallography software package. Journal of Applied Crystallography, 46, 544–549, https://doi.org/10.1107/S0021889813003531.
- Trumbo, S.K., Brown, M.E., and Hand, K.P. (2020) Endogenic and exogenic contributions to visible-wavelength spectra of Europa's trailing hemisphere. The Astronomical Journal, 160, 282, https://doi.org/10.3847/1538-3881/abc34c.
- Vu, T.H., Choukroun, M., Hodyss, R., and Johnson, P.V. (2020) Probing Europa's

- subsurface ocean composition from surface salt minerals using in-situ techniques. Icarus, 349, 113746, https://doi.org/10.1016/j.icarus.2020.113746.
- Wendt, L., Gross, C., Kneissl, T., Sowe, M., Combe, J.-P., LeDeit, L., McGuire, P.C., and Neukum, G. (2011) Sulfates and iron oxides in Ophir Chasma, Mars, based on OMEGA and CRISM observations. Icarus, 213, 86–103, https://doi.org/10.1016/ i.icarus.2011.02.013.
- Wildner, M., and Giester, G. (1991) The crystal structures of kieserite-type compounds. I. Crystal structures of Me(II)SO₄·H₂O (Me = Mn, Fe, Co, Ni, Zn). Neues Jahrbuch für Mineralogie - Neues Jahrbuch für Mineralogie. Abhandlungen, 7, 296–306.
- Wildner, M., Ende, M., Meusburger, J.M., Kunit, R., Matzinger, P., Talla, D., and Miletich, R. (2021) CoSO₄·H₂O and its continuous transition compared to the compression properties of isostructural kieserite-type polymorphs. Zeitschrift für Kristallographie. Crystalline Materials, 236, 225–237, https://doi.org/10.1515/zkri-2021-2038.
- Zhang, H., Tóth, O., Liu, X.-D., Bini, R., Gregoryanz, E., Dalladay-Simpson, P., De Panfilis, S., Santoro, M., Gorelli, F.A., and Martońák, R. (2020) Pressure-induced amorphization and existence of molecular and polymeric amorphous forms in dense SO₂. Proceedings of the National Academy of Sciences, 117, 8736–8742, https:// doi.org/10.1073/pnas.1917749117.

Manuscript received May 21, 2021 Manuscript accepted February 16, 2022 Accepted manuscript online March 3, 2022 Manuscript handled by Susannah Dorfman

Endnote:

¹Deposit item AM-23-38147, Online Materials. Deposit items are free to all readers and found on the MSA website, via the specific issue's Table of Contents (go to http://www.minsocam.org/MSA/AmMin/TOC/2023/Mar2023_data/Mar2023_data.html).